UC Berkeley
UC Berkeley Previously Published Works

Title

Adaptive-optics SLO imaging combined with widefield OCT and SLO enables precise 3D localization of fluorescent cells in the mouse retina

Permalink

https://escholarship.org/uc/item/0n67n81p

Journal

Biomedical Optics Express, 6(6)

ISSN

2156-7085

Authors

Zawadzki, Robert J
Zhang, Pengfei
Zam, Azhar
et al.

Publication Date

2015-06-01

DOI

10.1364/boe.6.002191

Peer reviewed

Adaptive-optics SLO imaging combined with widefield OCT and SLO enables precise 3D localization of fluorescent cells in the mouse retina

Robert J. Zawadzki,[1,2,6,9] Pengfei Zhang,[1] Azhar Zam,[1] Eric B. Miller,[3] Mayank Goswami,[1] Xinlei Wang,[1] Ravi S. Jonnal,[2] Sang-Hyuck Lee,[2] Dae Yu Kim,[4] John G. Flannery,[5] John S. Werner,[2] Marie E. Burns,[3,6] and Edward N. Pugh, Jr.[1,7,8]

[1]UC Davis RISE Eye-Pod Laboratory, Dept. of Cell Biology and Human Anatomy, University of California Davis, 4320 Tupper Hall, Davis, California 95616, USA
[2]Vision Science and Advanced Retinal Imaging Laboratory (VSRI) and Department of Ophthalmology & Vision Science, UC Davis, 4860 Y Street, Ste. 2400, Sacramento, CA 95817, USA
[3]Center for Neuroscience, University of California, Davis Sacramento, CA 95817, USA
[4]Beckman Laser Institute Korea & Biomed. Engineering, Dankook University, Cheonan, Chungnam 330-715, South Korea
[5]Dept. of Molecular and Cellular Biology, University of California, Berkeley 94720, USA
[6]Depts. of Ophthalmology & Vision Science and of Cell Biology & Human Anatomy 4303 Tupper Hall, Davis California 95616, USA
[7]Depts. of Cell Biology & Human Anatomy, and of Physiology & Membrane Biology 4303 Tupper Hall, Davis California 95616, USA
[8]enpugh@ucdavis.edu
[9]rjzawadzki@ucdavis.edu

Abstract: Adaptive optics scanning laser ophthalmoscopy (AO-SLO) has recently been used to achieve exquisite subcellular resolution imaging of the mouse retina. Wavefront sensing-based AO typically restricts the field of view to a few degrees of visual angle. As a consequence the relationship between AO-SLO data and larger scale retinal structures and cellular patterns can be difficult to assess. The retinal vasculature affords a large-scale 3D map on which cells and structures can be located during *in vivo* imaging. Phase-variance OCT (pv-OCT) can efficiently image the vasculature with near-infrared light in a label-free manner, allowing 3D vascular reconstruction with high precision. We combined widefield pv-OCT and SLO imaging with AO-SLO reflection and fluorescence imaging to localize two types of fluorescent cells within the retinal layers: GFP-expressing microglia, the resident macrophages of the retina, and GFP-expressing cone photoreceptor cells. We describe in detail a reflective afocal AO-SLO retinal imaging system designed for high resolution retinal imaging in mice. The optical performance of this instrument is compared to other state-of-the-art AO-based mouse retinal imaging systems. The spatial and temporal resolution of the new AO instrumentation was characterized with angiography of retinal capillaries, including blood-flow velocity analysis. Depth-resolved AO-SLO fluorescent images of microglia and cone photoreceptors are visualized in parallel with 469 nm and 663 nm reflectance images of the microvasculature and other structures. Additional applications of the new instrumentation are discussed.

References and links

1. D. R. Williams, "Imaging single cells in the living retina," Vision Res. **51**(13), 1379–1396 (2011).
2. D. P. Biss, D. Sumorok, S. A. Burns, R. H. Webb, Y. Zhou, T. G. Bifano, D. Côté, I. Veilleux, P. Zamiri, and C. P. Lin, "In vivo fluorescent imaging of the mouse retina using adaptive optics," Opt. Lett. **32**(6), 659–661 (2007).
3. C. Alt, D. P. Biss, N. Tajouri, T. C. Jakobs, and C. P. Lin, "An adaptive-optics scanning laser ophthalmoscope for imaging murine retinal microstructure," (2010), pp. 755019–755019–755011.
4. Y. Geng, A. Dubra, L. Yin, W. H. Merigan, R. Sharma, R. T. Libby, and D. R. Williams, "Adaptive optics retinal imaging in the living mouse eye," Biomed. Opt. Express **3**(4), 715–734 (2012).
5. R. Sharma, L. Yin, Y. Geng, W. H. Merigan, G. Palczewska, K. Palczewski, D. R. Williams, and J. J. Hunter, "In vivo two-photon imaging of the mouse retina," Biomed. Opt. Express **4**(8), 1285–1293 (2013).
6. L. Yin, Y. Geng, F. Osakada, R. Sharma, A. H. Cetin, E. M. Callaway, D. R. Williams, and W. H. Merigan, "Imaging light responses of retinal ganglion cells in the living mouse eye," J. Neurophysiol. **109**(9), 2415–2421 (2013).
7. J. Schallek, Y. Geng, H. Nguyen, and D. R. Williams, "Morphology and topography of retinal pericytes in the living mouse retina using in vivo adaptive optics imaging and ex vivo characterization," Invest. Ophthalmol. Vis. Sci. **54**(13), 8237–8250 (2013).
8. Y. Jian, R. J. Zawadzki, and M. V. Sarunic, "Adaptive optics optical coherence tomography for in vivo mouse retinal imaging," J. Biomed. Opt. **18**(5), 056007 (2013).
9. Y. Jian, J. Xu, M. A. Gradowski, S. Bonora, R. J. Zawadzki, and M. V. Sarunic, "Wavefront sensorless adaptive optics optical coherence tomography for in vivo retinal imaging in mice," Biomed. Opt. Express **5**(2), 547–559 (2014).
10. B. N. Giepmans, S. R. Adams, M. H. Ellisman, and R. Y. Tsien, "The fluorescent toolbox for assessing protein location and function," Science **312**(5771), 217–224 (2006).
11. Y. Geng, L. A. Schery, R. Sharma, A. Dubra, K. Ahmad, R. T. Libby, and D. R. Williams, "Optical properties of the mouse eye," Biomed. Opt. Express **2**(4), 717–738 (2011).
12. D. A. Hume, V. H. Perry, and S. Gordon, "Immunohistochemical localization of a macrophage-specific antigen in developing mouse retina: phagocytosis of dying neurons and differentiation of microglial cells to form a regular array in the plexiform layers," J. Cell Biol. **97**(1), 253–257 (1983).
13. E. S. Levine, A. Zam, P. Zhang, A. Pechko, X. Wang, P. FitzGerald, E. N. Pugh, Jr., R. J. Zawadzki, and M. E. Burns, "Rapid light-induced activation of retinal microglia in mice lacking Arrestin-1," Vision Res. **102**, 71–79 (2014).
14. A. Z. Zam, E. N. Pugh Jr., and R. J. Zawadzki, "Evaluation of OCT for quantitative in vivo measurements of changes in neural tissue scattering in longitudinal studies of retinal degeneration in mice," Proceedings of SPIE BiOS: Optical Coherence Tomography and Coherence Domain Optical Methods in Biomedicine **8934**, 6 (2014).
15. M. Wojtkowski, V. Srinivasan, T. Ko, J. Fujimoto, A. Kowalczyk, and J. Duker, "Ultrahigh-resolution, high-speed, Fourier domain optical coherence tomography and methods for dispersion compensation," Opt. Express **12**(11), 2404–2422 (2004).
16. J. Fingler, D. Schwartz, C. Yang, and S. E. Fraser, "Mobility and transverse flow visualization using phase variance contrast with spectral domain optical coherence tomography," Opt. Express **15**(20), 12636–12653 (2007).
17. J. Fingler, R. J. Zawadzki, J. S. Werner, D. Schwartz, and S. E. Fraser, "Volumetric microvascular imaging of human retina using optical coherence tomography with a novel motion contrast technique," Opt. Express **17**(24), 22190–22200 (2009).
18. D. Y. Kim, J. Fingler, J. S. Werner, D. M. Schwartz, S. E. Fraser, and R. J. Zawadzki, "In vivo volumetric imaging of human retinal circulation with phase-variance optical coherence tomography," Biomed. Opt. Express **2**(6), 1504–1513 (2011).
19. D. Y. Kim, J. Fingler, R. J. Zawadzki, S. S. Park, L. S. Morse, D. M. Schwartz, S. E. Fraser, and J. S. Werner, "Optical imaging of the chorioretinal vasculature in the living human eye," Proc. Natl. Acad. Sci. U.S.A. **110**(35), 14354–14359 (2013).
20. P. F. Zhang, A. Zam, E. N. Pugh, and R. J. Zawadzki, "Evaluation of state-of-the-art imaging systems for in vivo monitoring of retinal structure in mice: current capabilities and limitations," Ophthalmic Technologies Xxiv. 8930, (2014).
21. S. H. Lee, J. S. Werner, and R. J. Zawadzki, "Improved visualization of outer retinal morphology with aberration cancelling reflective optical design for adaptive optics - optical coherence tomography," Biomed. Opt. Express **4**(11), 2508–2517 (2013).
22. R. J. Zawadzki, S. M. Jones, S. Pilli, S. Balderas-Mata, D. Y. Kim, S. S. Olivier, and J. S. Werner, "Integrated adaptive optics optical coherence tomography and adaptive optics scanning laser ophthalmoscope system for simultaneous cellular resolution in vivo retinal imaging," Biomed. Opt. Express **2**(6), 1674–1686 (2011).
23. R. S. Jonnal, O. P. Kocaoglu, R. J. Zawadzki, S. H. Lee, J. S. Werner, and D. T. Miller, "The cellular origins of the outer retinal bands in optical coherence tomography images," Invest. Ophthalmol. Vis. Sci. **55**(12), 7904–7918 (2014).
24. A. Roorda, "Adaptive optics for studying visual function: a comprehensive review," J. Vis. **11**(5), 6 (2011).

25. S. Bonora, G. Naletto, R. Zawadzki, S. Residori, and U. Bortolozzo, *Devices and Techniques for Sensorless Adaptive Optics* (INTECH Open Access Publisher, 2012).
26. R. J. Zawadzki, S. M. Jones, S. S. Olivier, M. Zhao, B. A. Bower, J. A. Izatt, S. Choi, S. Laut, and J. S. Werner, "Adaptive-optics optical coherence tomography for high-resolution and high-speed 3D retinal in vivo imaging," Opt. Express **13**(21), 8532–8546 (2005).
27. S. Jung, J. Aliberti, P. Graemmel, M. J. Sunshine, G. W. Kreutzberg, A. Sher, and D. R. Littman, "Analysis of fractalkine receptor CX(3)CR1 function by targeted deletion and green fluorescent protein reporter gene insertion," Mol. Cell. Biol. **20**(11), 4106–4114 (2000).
28. D. Dalkara, L. C. Byrne, R. R. Klimczak, M. Visel, L. Yin, W. H. Merigan, J. G. Flannery, and D. V. Schaffer, "In vivo-directed evolution of a new adeno-associated virus for therapeutic outer retinal gene delivery from the vitreous," Sci. Transl. Med. **5**(189), 189ra76 (2013).
29. Y. Wang, J. P. Macke, S. L. Merbs, D. J. Zack, B. Klaunberg, J. Bennett, J. Gearhart, and J. Nathans, "A locus control region adjacent to the human red and green visual pigment genes," Neuron **9**(3), 429–440 (1992).
30. Y. Fei and T. E. Hughes, "Transgenic expression of the jellyfish green fluorescent protein in the cone photoreceptors of the mouse," Vis. Neurosci. **18**(4), 615–623 (2001).
31. D. M. Schwartz, J. Fingler, D. Y. Kim, R. J. Zawadzki, L. S. Morse, S. S. Park, S. E. Fraser, and J. S. Werner, "Phase-variance optical coherence tomography: a technique for noninvasive angiography," Ophthalmology **121**(1), 180–187 (2014).
32. J. Canny, "A computational approach to edge detection," IEEE Trans. Pattern Anal. Mach. Intell. **8**(6), 679–698 (1986).
33. W. T. Freeman and E. H. Adelson, "The Design and Use of Steerable Filters," IEEE Trans. Pattern Anal. Mach. Intell. **13**(9), 891–906 (1991).
34. M. Jacob and M. Unser, "Design of steerable filters for feature detection using canny-like criteria," IEEE Trans. Pattern Anal. Mach. Intell. **26**(8), 1007–1019 (2004).
35. B. F. Hochheimer, G. A. Lutty, and S. A. D'Anna, "Ocular fluorescein phototoxicity," Appl. Opt. **26**(8), 1473–1479 (1987).
36. A. Mishra, F. M. O'Farrell, C. Reynell, N. B. Hamilton, C. N. Hall, and D. Attwell, "Imaging pericytes and capillary diameter in brain slices and isolated retinae," Nat. Protoc. **9**(2), 323–336 (2014).
37. A. Roorda, F. Romero-Borja, W. Donnelly Iii, H. Queener, T. Hebert, and M. Campbell, "Adaptive optics scanning laser ophthalmoscopy," Opt. Express **10**(9), 405–412 (2002).
38. J. Tam, J. A. Martin, and A. Roorda, "Noninvasive visualization and analysis of parafoveal capillaries in humans," Invest. Ophthalmol. Vis. Sci. **51**(3), 1691–1698 (2010).
39. T. Y. Chui, D. A. Vannasdale, and S. A. Burns, "The use of forward scatter to improve retinal vascular imaging with an adaptive optics scanning laser ophthalmoscope," Biomed. Opt. Express **3**(10), 2537–2549 (2012).
40. Z. Zhong, H. Song, T. Y. Chui, B. L. Petrig, and S. A. Burns, "Noninvasive measurements and analysis of blood velocity profiles in human retinal vessels," Invest. Ophthalmol. Vis. Sci. **52**(7), 4151–4157 (2011).
41. J. B. Schallek, H. N. Nguyen, C. Schwarz, and D. R. Williams, "Non-invasive Adaptive Optics Imaging of Retinal Pericytes and Capillary Blood Velocity in Mice," J. Vis. **12**(14), 50 (2012).
42. C. Alt, J. M. Runnels, L. J. Mortensen, W. Zaher, and C. P. Lin, "In vivo imaging of microglia turnover in the mouse retina after ionizing radiation and dexamethasone treatment," Invest. Ophthalmol. Vis. Sci. **55**(8), 5314–5319 (2014).
43. L. D. Carter-Dawson and M. M. LaVail, "Rods and cones in the mouse retina. I. Structural analysis using light and electron microscopy," J. Comp. Neurol. **188**(2), 245–262 (1979).
44. C. A. Curcio, K. R. Sloan, R. E. Kalina, and A. E. Hendrickson, "Human photoreceptor topography," J. Comp. Neurol. **292**(4), 497–523 (1990).
45. S. S. Nikonov, R. Kholodenko, J. Lem, and E. N. Pugh, Jr., "Physiological features of the S- and M-cone photoreceptors of wild-type mice from single-cell recordings," J. Gen. Physiol. **127**(4), 359–374 (2006).
46. F. Naarendorp, T. M. Esdaille, S. M. Banden, J. Andrews-Labenski, O. P. Gross, and E. N. Pugh, Jr., "Dark light, rod saturation, and the absolute and incremental sensitivity of mouse cone vision," J. Neurosci. **30**(37), 12495–12507 (2010).
47. J. A. Peet, A. Bragin, P. D. Calvert, S. S. Nikonov, S. Mani, X. Zhao, J. C. Besharse, E. A. Pierce, B. E. Knox, and E. N. Pugh, Jr., "Quantification of the cytoplasmic spaces of living cells with EGFP reveals arrestin-EGFP to be in disequilibrium in dark adapted rod photoreceptors," J. Cell Sci. **117**(14), 3049–3059 (2004).
48. M. L. Applebury, M. P. Antoch, L. C. Baxter, L. L. Chun, J. D. Falk, F. Farhangfar, K. Kage, M. G. Krzystolik, L. A. Lyass, and J. T. Robbins, "The murine cone photoreceptor: a single cone type expresses both S and M opsins with retinal spatial patterning," Neuron **27**(3), 513–523 (2000).
49. L. L. Daniele, C. Insinna, R. Chance, J. Wang, S. S. Nikonov, and E. N. Pugh, Jr., "A mouse M-opsin monochromat: retinal cone photoreceptors have increased M-opsin expression when S-opsin is knocked out," Vision Res. **51**(4), 447–458 (2011).

1. Introduction

Over the last decade, the development of adaptive optics (AO) instruments has made it possible to routinely image the human retina *in vivo* at cellular resolution [1]. However, reports of *in vivo* imaging of the mouse retina with AO-enhanced SLO and OCT have only

recently been published [2–9]. AO imaging of the mouse retina has been delayed by the challenge of designing a system for an eye ten-fold smaller than that of the human, and by the availability of highly developed *ex vivo* histochemical retinal imaging methods. Such methods cannot report the properties and functions of living tissue, and moreover are also relatively expensive inasmuch as they require cohorts of experimental and control animals, often for each of a number of time points in a study. AO-imaging of the mouse eye can be seen as part of an ongoing revolution in biological imaging, which is aimed at visualizing cellular structure and function *in vivo*, particularly with genetically encoded optical probes [10]. Remarkably, the mouse eye has an AO-corrected numerical aperture of ~0.5, exceeding that of the human eye by ~2.5-fold [4, 11], affording exquisite submicron resolution.

Here we describe an AO-SLO instrument for reflectance and fluorescence imaging of the mouse retina based on the general design of Geng et al. [4]. We demonstrate its utility by imaging retinal capillaries, retinal blood flow, and microglia and cone photoreceptor cells that constitutively express GFP, and show how these structures and cells can be localized in 3D by combining the AO-SLO data with widefield OCT/pv-OCT and SLO data. Consistent with previous histological studies [12, 13], AO-SLO imaging shows the microglia to reside primarily in the neurofibrillary and plexiform layers, and show that two distinct regions of cone cell GFP fluorescence can be distinguished, corresponding to the pedicles of the outer plexiform and the cell body and inner segment near the external limiting membrane.

2. Materials and methods

This section provides a brief description of the experimental systems, and methods used to evaluate volumetric retinal structures of the mouse eye.

2.1 Widefield in vivo mouse retinal imaging

2.1.1 OCT/pv-OCT

To acquire volumetric morphology and vascular maps of the mouse retina a custom OCT system was constructed [14]. The OCT system utilizes Fourier-Domain OCT (Fd-OCT) with a broad bandwidth superluminescent diode (SLD, Broadlighter T-860-HP; Superlum, Carrigtwohill, Cork, Ireland, λ_0 = 855 nm, $\Delta\lambda$ = 132 nm, and P_{out} = 15 mW) as a light source an OCT spectrometer comprising a holographic diffraction grating (1200 l/mm @ 840 nm; Wasatch Photonics, Inc. Duhram, NC, USA), an imaging objective (Zeiss 85 mm f1.4 Planar ZF-IR; Zeiss. Jenna, Germany) and a CMOS camera (spL4096-140km; Basler AG, Ahrensburg, Germany) operating up to 100,000 A-scan/s as its detector. The sample arm was attached to a probe unit, which comprises a fiber collimator lens (Thorlabs, Inc. Newton, NJ, USA), two single-axis galvanometric scanners (6215HM; Cambridge Technology, Inc. Bedford, MA, USA), and three achromatic doublets as the scanning lens (Edmund Optics, Inc Barrington, NJ, USA). The reference arm of the fiber coupler is attached to an OCT reference arm unit comprising a fiber collimator lens, an achromatic doublet lens, neutral density filter, dispersion-compensating block and a static silver-coated mirror. The OCT system has theoretical axial resolution of ~2 μm in the mouse eye, and a lateral resolution of ~5 μm (FWHM). OCT images could be acquired over 41 deg of visual angle (~1.4 mm). In converting angles to retinal distances in this manuscript, we use the conversion factor 34 μm/deg, corresponding to a posterior nodal distance of 1.95 mm. The Fd-OCT system collects a spectral fringe pattern that is processed using standard Fd-OCT methods to reconstruct both amplitude and phase information [15]. Different scanning patterns have been used to acquire OCT images presented in this paper. The two most frequently used included: 100 B-scans with 2000 A-scans/B-scan (25 frames/s) for standard OCT, and 360 clusters of 4 B-scans with 360 A-scan/B-scan (250 frames/s) for phase-variance OCT (pv-OCT). Phase-variance contrast analysis of pv-OCT volumes was performed as previously described [16–19]. Briefly, phase changes were calculated for the entire cross-sectional image from consecutively

acquired sets of three B-scans (BM-scans). Bulk axial motion for each B-scan was calculated and corrected for each set of BM-scans, reducing the phase noise created by mouse eye movements. Intensity thresholding based on the average OCT intensity B-scan was used to create a mask for the pv-OCT image that removed contributions of phase noise caused by low signal-to-noise regions. Combined OCT and pv-OCT analysis generated a volumetric morphology of the retinal layers and microvasculature which were used as a reference map for localizing blood vessels and cells in 3D with AO-SLO imaging.

2.1.2 Widefield scanning laser ophthalmoscope (SLO)

A custom-built, multichannel SLO system [20] was used to acquire widefield (50 deg visual angle, 1.7 mm) reflectance and fluorescence images. These images were used in combination with pv-OCT imaging of the retinal vasculature, described above, as maps on which fluorescent cells and other retinal features were located for higher resolution (but necessarily much smaller FOV) AO-SLO imaging. A key feature of this SLO is a sensitive spectrum analyzer (Ocean Optics™ QE65000), used for spectral emission fingerprinting of fluorescence cells and autofluorescence.

2.2 AO-SLO

We previously described a clinical imaging AO-OCT system that uses an optical design based on reflective optics to minimize system aberrations and pupil wander [21]. Here we present an AO-SLO system for small animal imaging built upon the same principles, including modifications necessary for mouse retinal imaging.

2.2.1 Optical design of AO-SLO system

The physical layout of the imaging optics of the AO-SLO is illustrated to scale in Fig. 1.
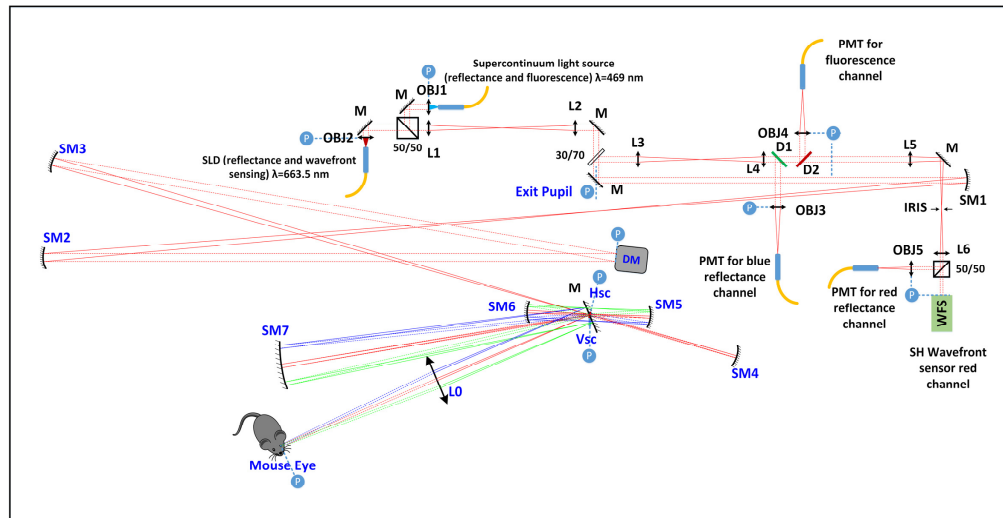

Fig. 1. Optical layout of the AO-SLO system. The layout is presented in a scale drawing, and the precise x-, y- and z- locations of each element are presented in Table 1. Abbreviations: L#, lens; M, mirror; SM, spherical mirror; DM, deformable mirror; D#, dichroic mirror; OBJ, focusing objective lens; Hsc, horizontal resonant scanner; Vsc, vertical scanner; PMT, photomultiplier tube; P (circled in blue) optical planes conjugate with the pupil; SLD, superluminescent diode. Collimated beams are marked as dashed lines and focusing beams are marked as solid lines. The on-axis beams are represented by red lines and scanned beams by green and blue.

We used a cascade of focal telescopes created by pairs of spherical mirrors to produce multiple planes conjugate with the eye pupil for all key optical components, including the x-

and y- scanning mirrors, the wavefront corrector and a Shack-Hartmann wavefront sensor (SHWS). This design is similar to that of the AO-SLO system for mouse retinal imaging presented by Geng et al. [4], in that a large focal length achromatic lens (L0; L-AOC156, Ross Optical, El Paso, Texas) is used as the last optical element prior to the contact lens. The principal differences are that the deformable mirror (DM) is located closer to the wavefront sensor, and the mouse contact lens (0 Dpt.) (Unicon Corporation, Osaka, Japan) was mounted at the pupil plane of the system to improve the repeatability of imaging sessions. The field of view (FOV) and defocus correction range that affords diffraction-limited performance is similar to that presented by Geng et al. [4].

Table 1. Design parameters of optical system (Focal length, x, y and z position, pupil size)

Surface #	Focal length (mm)	Position x (mm)	Position y (mm)	Height z (mm)	Aperture size (mm)
Exit Pupil	-	0	0	51	9
SM1	1000	1000	0	51	-
SM2	1500	−1477	−304	197	-
Deformable Mirror	-	21	−278	127	13.5
SM3	1350	−1311	−68	63	-
SM4	375	354	−514	123	-
Horizontal Scanner (H_{SC})	-	−7	−417	94	3.75
SM5	150	143	−420	83	-
SM6	150	−152	−414	136	-
Vertical Scanner (V_{SC})	-	−3	−417	131	3.75
SM7	762	−742	−587	199	-
Flat mirror (M)	-	0	−416	201	-
Lens (L0)	400	−373	−573	201	-
Entrance Pupil (mouse eye)	-	−753	−732	201	1.95

The current AO-SLO uses light from two spectral bands for imaging: the one for back-reflection and fluorescence imaging was typically centered at 469 nm (filtered by Semrock bandpass filter FF01-469/35) from a supercontinuum light source (Fianium[TM], WL-SC400-4); and, the second, used for both reflectance imaging and wavefront sensing was centered at 663 nm (from a superluminescent diode (SLD-26-HP; Superlum, Carrigtwohill, Cork, Ireland, λ_0 = 663.5 nm, $\Delta\lambda$ = 6.8 nm, and P_{out} = 5 mW). In the description below we shall refer to the two beams as the "blue" and "red" channel, respectively. At the mouse pupil plane the beams were ~2 mm in diameter, defined by the aperture of the deformable mirror. The intensity profiles of the beams are described by the central part of a Gaussian beam truncated by the circular aperture (DM). For the wavefront beacon an additional small circular stop in the center of the beam was used to generate an annular beam profile that helped reduce back reflection artifacts seen by the SHWS [4].

The AO-SLO employs a resonant scanner (SC-30, Electro-Optical Products Corp. Fresh Meadows, NY) operating at 14 KHz, and collects square image frames (512x512 pixels) at 23 Hz. The FOV can be varied, ranging up to a maximum of 8 deg visual angle. Images presented in this manuscript were acquired with a FOV of 3 or 6 deg. For some experiments the system was operated in "linescan" mode, with the line of scanning centered in x-y frames collected immediately before and/or after the line scanning commenced.

2.2.2 Optical performance of AO-SLO system

The optical system was designed with Zemax^{TM} software, which was also used to characterize its performance. Achieving diffraction-limited performance in the largest possible field of view was the overarching goal of the design. The size of the mouse eye and the size of the wavefront corrector necessarily constrained the design. Table 1 provides the positions of all the optical components that affect performance. The design software was employed to achieve minimum wavefront error and pupil wander for an 8 x 8 deg FOV.

A. Wavefront error

B. Pupil wander
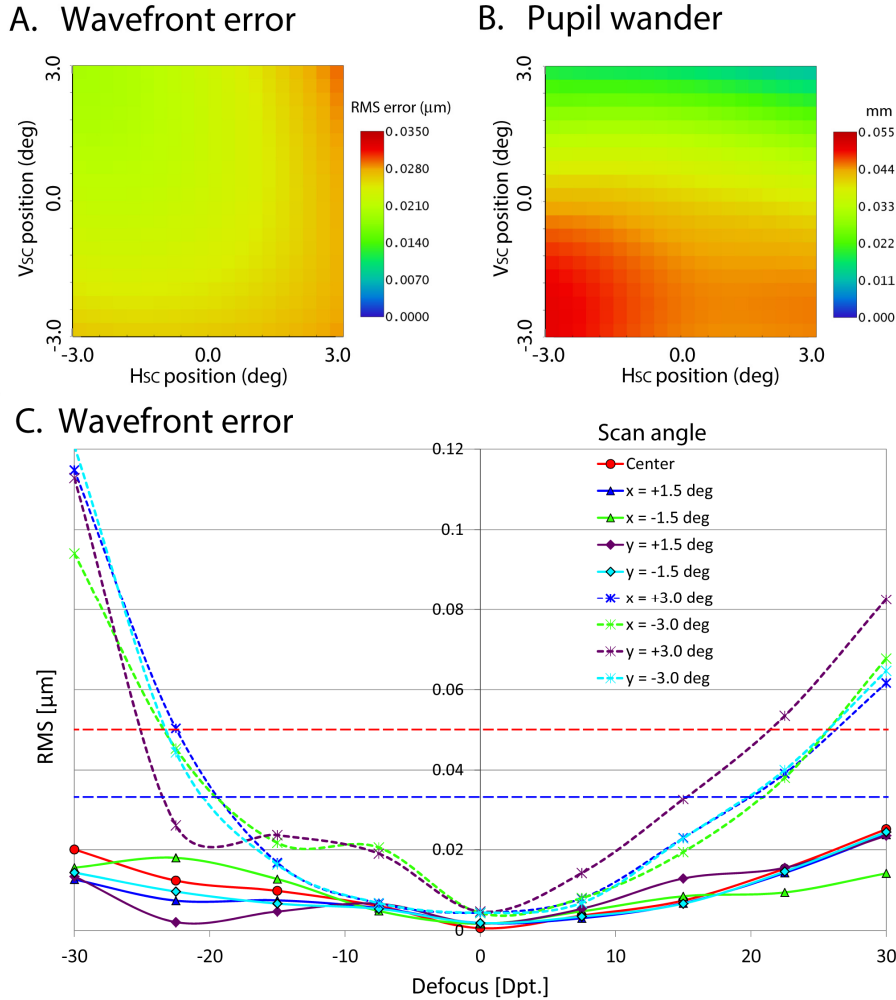
C. Wavefront error

Fig. 2. Optical performance of our AO-SLO system as a function of imaging beam position in x- and y-axis (mechanical angle of H_{SC} and V_{SC}) on the mouse retina over 6 deg x 6 deg (200 µm x 200 µm). **A.** RMS wavefront error. **B.** Pupil wander. **C.** RMS wavefront error of the AO-SLO system after correction for defocus at the entrance pupil by the Deformable Mirror (one DM shape for one Defocus value), evaluated on axis and at the four extremes of the full scanning range of 3 deg (± 1.5 deg) and 6 deg (± 3.0 deg). Dashed horizontal lines represent diffraction limited RMS (λ/13.4) for 469 nm (blue) and 663 nm (red) wavelength (35 nm and 49.5 nm respectively). Note, that these simulations do not take into account the optical aberrations of the mouse eye, which necessarily reduces system performance.

The root mean square (RMS) wavefront error of the whole system with the DM simulated as a flat mirror is plotted as a function of scanning mirrors' positions in Fig. 2(A). The maximum wavefront error is under 35 nm for the whole field (λ/13.4, diffraction limit for λ =

469 nm; minimum Strehl ratio 0.8). The relatively small RMS error of the system allows the entire stroke of the wavefront-correcting DM to be used for correcting aberrations of the mouse's eye, rather than correcting for imperfections in the optical system itself. Another important parameter taken into account during optical design was reduction of pupil wander at the system entrance pupil plane (mouse eye pupil plane). The predicted maximum pupil wander is under 50 μm (2.5%) as shown in Fig. 2(B). We have confirmed that value by measuring pupil wander in the pupil plane conjugate to the vertical and horizontal scanners by placing a CMOS detector in that plane and recording the pupil position during 6 deg scanning in each direction. The AO-SLO was designed to achieve diffraction-limited performance for defocus of the mouse eye ranging from −30 to + 30 Diopter (Dpt) with a 3 x 3 deg field of view. One needs about 50 Dpt to shift the axial focus over the total thickness of the mouse retina (~220 μm) [4]. Thus, this diffraction-limited defocus correction range also defines the axial focus shift available in our AO system.

2.2.3 Adaptive optics

The AO system incorporated a custom Shack-Hartmann wavefront sensor (SHWS) consisting of a lenslet array (10 mm x 10 mm, Pitch = 150 μm, f = 6.7 mm; MLA150-7AR, Thorlabs, Newton, New Jersey) and sCMOS detector (2048 × 2048 pixel; Ace acA2040-180 km; Basler AG), and a high-speed, high-stroke deformable mirror (DM; DM-97-15; ALPAO SAS, Montbonnot St. Martin, France). The AO system was limited by centroid computation time, and ran at 16 Hz using the full 4 megapixel spots image. The pupil diameters are 2 mm, 13.5 mm, and 4.5 mm at the mouse eye, the DM, and the SHWS, respectively. The pupil diameter at the SHWS defined a circular aperture having a diameter of 30 lenslets, and a total of 700 spots used for centroiding.

Diffraction-limited imaging as defined by the RMS error of the measured wavefront was routinely achieved ($\sigma_{Zernike}$ < 50 nm). This performance corresponds to a theoretical lateral resolution of 0.75 μm for the red beam on the retina. Custom software was used for both the SLO control and data acquisition system, and for the AO-correction system. The SLO software was written in C++ , and provided real-time viewing of the acquired images [22]. The AO software was written in Python/NumPy [23]. The two systems run on separate PCs. The AO software provided real-time wavefront reconstruction and residual error feedback, informing operators when the correction was diffraction-limited. Because the contact lens was mounted in the system entrance pupil plane, the mouse axial position could be adjusted to bring the desired retinal layer into focus for the DM set to flat mode (no aberration correction). Once the layer of interest was in focus no further changes to the mouse's axial position were made. This procedure ensured that the DM stroke was used mostly for higher order aberration correction. The AO system also provided a method for dynamically adding positive or negative defocus by modifying the SHWS reference coordinates, as now described.

Adaptive optics can be used not only to correct aberration in the imaging system, but also to generate desired aberrations. This is often used in aberration-dependent vision testing [24] or image quality-based aberration correction [25]. In our AO-SLO, similar to other AO-based imaging systems, this feature was used to actively shift the axial focus position of the imaging beam by adding a prescribed defocus term to the AO reference control, modifying the shape of the deformable mirror [26]. As a consequence, the focal plane of the AO beacon was allowed to move away from the photoreceptor layer during AO correction and imaging, unlike the approach used by Geng et al. [4]. Thus, we allowed our red AO beacon to shift axially with the blue imaging beam. When the focus was shifted in this manner, the red reflection channel image was used to assess the axial location of focus, and also together with the dynamically reported AO-residual RMS error, the correction quality. While this changing of the axial focus position of the AO beacon sometimes resulted in suboptimal wavefront sensing and correction, it nonetheless provided an efficient means for changing the focus of

the imaging beam, allowing rapid imaging of several depth planes. This focusing method works linearly with the defocus of the AO system when imaging structures near the photoreceptor layer. For imaging structures near the NFL such as microvasculature and axon fiber bundles the AO reference plane would jump smoothly from the photoreceptor layer to the NFL, the highest reflecting structure in the inner retina [11]. However based on an understanding of mouse retinal anatomy, on prior OCT and pv-OCT imaging of the individual mouse, and on the availability of the red reflectance imaging channel, this effect could be easily compensated in offline analysis to recover the precise axial depth.

The ability of the AO control software to rapidly shift focus enabled the application of a special "dynamic focusing" control mode, in which the operator specifies the starting and ending amplitude of the defocus term, as well as the number of steps between these two positions. Once executed, the AO system shifts the focus smoothly between the two specified points with reference defocus updated for each consecutive AO-loop. For example, with the current AO loop update rate of 16 Hz and 200 steps over an axial range of dynamic focus, it takes 12.5 s (about 300 frames) to image the whole range. This dynamic focusing mode was used to acquire image z-stacks. As noted by Geng et al. [11], a limitation of this method is that the mouse retina has two distinct high reflectance layers that can each serve as the focus of the wavefront sensing beacon [11], and during z-stack the wavefront sensing can shift from the inner retinal reflectance to the outer one. Use of OCT data obtained from the same mouse, however, enabled us to determine the AO-SLO focus plane for each nominal z-position, as described in the Results.

2.2.4 AO-SLO data acquisition

Reflected or fluorescent light from the mouse retina was separated by 2 dichroic mirrors (FF509-FDi01 and FF640-FDi01, Semrock) into 3 non-overlapping bands: (i) $\lambda < 509$ nm for "blue channel" back-reflection imaging; (ii) 509 nm $< \lambda <$ 640 nm for fluorescence imaging (with an additional band-pass filter FF01-525/45 for GFP fluorescence); (iii) $\lambda > 640$ nm for "red channel" back-reflectance imaging and wavefront sensor, with the latter further filtered (FL670-10, Thorlabs). The light from the back-reflection and fluorescence channels was collected by selectable optical fibers (typically, with an aperture of 4 Airy discs), and then passed to PMTs (H7422-50 for back-reflection, and H7422-40 for fluorescence, Hamamatsu Photonics), and amplified for transfer to the data acquisition system. The positions of the "blue channel" light source fiber, "blue channel" back-reflectance detection pinhole and fluorescence imaging pinhole were adjusted during imaging to cancel chromatic shift created by chromatic aberrations present in the system and in the mouse eye. As a result, both blue and red beams were focused at the same axial plane on the retina and all three detection channels recorded images from the same retinal plane.

2.3 Mouse strains and handling

All animals were handled according to the guidelines of the University of California Davis Institutional Animal Care and Use Committee (IACUC). Mice were anesthetized with 2-3% isofluorane delivered in O_2, the pupils were dilated and cyclopleged with tropicamide and phenylephrine. Gel Tears with 0.2% carbomer (Chem-Pharm Fabrik, Berlin, DE) was applied between the corneal surface and the custom 0 Dpt contact lens (Unicon Corporation, Osaka, Japan) to moisturize the eye and also maintain a homogeneous refractive surface. The anesthetic delivery system included a "bite bar" mounted on a micropositioner (Bioptigen, Morrisville, NC) with rotational and translational degrees of freedom for positioning the mouse with respect to the contact lens. All mice were obtained from Jackson Labs. Three mouse variants were used in this study: (1) wild type (WT) mice (C57Bl/6); (2) $Cx3cr1^{GFP/+}$ mice, which have the gene for enhanced green fluorescent protein (EGFP) knocked into the locus of the $Cx3cr1$ gene, causing EGFP to be constitutively expressed in the central nervous system primarily in microglia cells [27] and, (3) mice with cones that express EGFP. The

latter mice were produced from WT mice by intravitreal injection (0.5 μL) of a custom adenovirus capsid (AAV-7M8 [28];) packaged with a DNA construct comprising the human L/M opsin promoter (hLM) driving EGFP expression [29, 30]. Fluorescein angiography was performed on animals after tail-vein injection of 50 μL clinical grade AK-Fluor 10% (Akorn).

2.4 Image processing and analysis

Raw mouse OCT data were processed as previously described [13, 14]. Phase-variance analysis (pv-OCT) was performed as described previously [18, 31]. Raw AO-SLO scan data were corrected for the sinusoidal motion of the resonant scanning mirror. Most other post-processing was performed with tools available in ImageJ software (Fiji version), including alignment of successive images in stacks, averaging, contrast adjustment, and extracting distance parameters. Custom scripts written in Matlab^{TM} were used for some analyses, including interpolation of z-stack data on a uniform axial micrometer scale, and extracting the velocity of blood cell flow. For blood flow analysis, we employed a steerable 2D filter to extract "particle tracks" in x-t images [32–34]. Thus, each x-t image was convolved with a series of rotated versions of a 2D Gaussian reference template. Rotation of the filter was effected by means of weighted linear combinations of the reference template [34].

3. Results

3.1 OCT imaging and phase-variance analysis used as a roadmap for AO-SLO imaging

3.1.1 OCT volumes

OCT volumes comprising 100 B-scans each in turn comprising 2000 A-scans (lines) were acquired over 41 deg of visual angle at an acquisition speed of 25 B-scans/s. Figure 3(B) illustrates an *en face* projection of a standard OCT volume, while panel A shows the B-scan image corresponding to the red arrow in B. The various retinal layers and layer boundaries are readily identified in the B-scan.

3.1.2 Phase-variance-OCT

The OCT volume data set shown in Fig. 3(B) was subjected to phase-variance analysis [16, 18, 19]. This analysis can reveal the entire vasculature in the OCT volume, including the finest capillaries (Fig. 3(C)). The high axial resolution of the OCT system (~2 μm) enables the axial position of the vessels to be precisely determined, as illustrated in panel D, where the depth level has been color coded, ranging from the neurofibrillary level (NFL, blue) to the outer plexiform layer (OPL, red). Pv-OCT is ideal for obtaining a 3D angiographic map of the outer retina, inasmuch as it is a label-free technique that employs generally harmless near-infrared light. In contrast, fluorescein, commonly used for retinal angiography, requires blue-green excitation and can produce photo-oxidative damage [35]. Note that in Media 2, which presents a 3D rendering of the data in Fig. 3(D), an axial motion artifact due to movement of the mouse's eye during pv-OVT data acquisition can be seen in the side view. This axial motion artifact can be readily accounted for when interpreting depth positions of the retinal vasculature in pv-OCT data sets. The axial movement in Fig. 3(D) is smaller than the distance between two capillary plexus and thus will not cause confusion. If needed, any of many OCT volume motion correction methods could be used to remove this artifact.
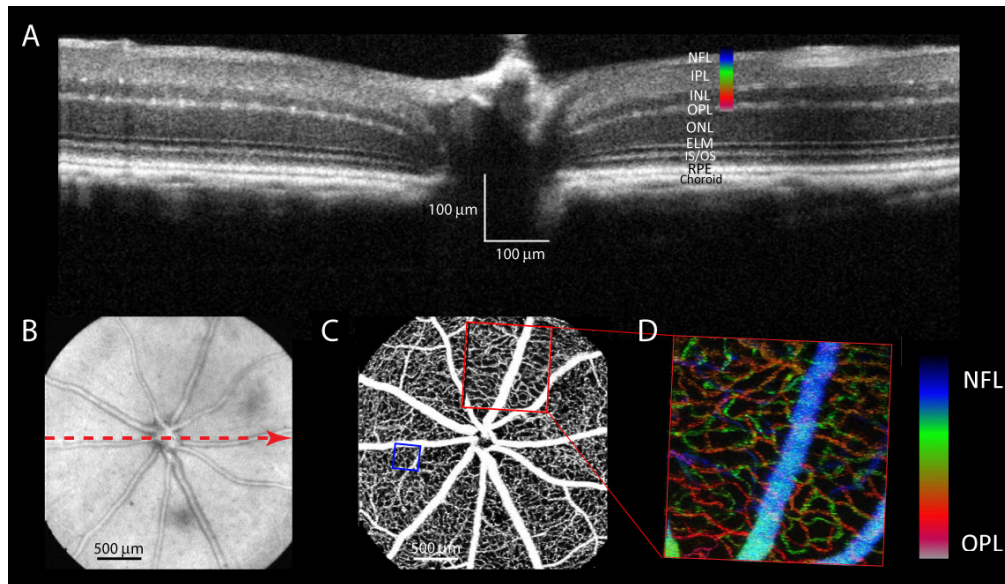
Fig. 3. OCT imaging and phase-variance (pv-) analysis reveals the mouse retinal vascular bed. **A.** B-scan centered on the optic nerve corresponding to the red dashed arrow in B (note 1:1 x-y scaling). The retinal layer and boundary identifications are: NFL neurofibrillary layer); IPL (inner plexiform layer); INL (inner nuclear layer); OPL (outer plexiform layer); ONL (outer nuclear layer); ELM (external limiting membrane); IS/OS (photoreceptors' inner segment/outer segment junctions); RPE (retinal pigment epithelium**). B.** *En face* projection of the OCT volume (41 deg visual angle, 1400 µm diameter) centered on the optic nerve and illustrating the major blood vessels (Media 1 presents a rendering of the full volume). **C.** *En face* projection of the phase variance analysis of the OCT volume of panel B. **D.** High resolution pv-OCT image of the region in the red box in C; the vessel depth has been color coded as indicated in panel A (Media 2 presents a 3D rendering of the image in D). Blue box in C represents the location of the AO-SLO scan that is discussed in detail in Fig. 4.

3.2 AO-SLO imaging of the retinal vasculature

3.2.1 Lateral and axial resolution of the AO-SLO system

To examine the resolution of the AO-SLO, we performed fluorescein angiography of the retinal capillary bed in "z-stack" dynamic focus mode (Fig. 4). These results were obtained from the same mouse and eye already illustrated in Fig. 3: the precise location of the z-stack in the mouse fundus was determined by matching the fluorescence angiogram pattern with the pv-OCT angiogram (Fig. 3(C), blue box). More generally, any desired location in the central retina could be found for AO-SLO imaging by "navigating" along a previously obtained pv-OCT or widefield SLO map: thus, the mouse was moved with the micro-positioning device so as to keep vascular landmarks in the map in view. The theoretical depth of focus for our AO-SLO system in the diffraction-limited case at 469 nm is approximately 5 µm. The very clear differences between the fluorescence images obtained at different z-positions (Fig. 4(A)-4(C)) demonstrate that the AO-SLO is functioning as a confocal system with useful z-resolution, and allowed unequivocal determination of the retinal layer of the fluorescent blood vessels. Moreover, by comparing the pv-OCT and AO-SLO maps of the blood vessels at different depths, we determined the relationship between the AO-SLO z-position "focus depth" and the actual retinal depth (Fig. 4(D)), and used this relationship to generate by interpolation a z-stack calibrated in micrometers (Fig. 4(E)). This is a useful method of calibrating the dynamic focus control of the AO-SLO.

To assess the lateral resolution of the AO-SLO, we measured fluorescence intensity profiles along lines perpendicular to the smallest capillaries at the z-position of their

maximum image width in the z-stack (Fig. 4(B), 4(D)). The average full width half-maximum (FWHM) along such profiles was 5.7 ± 0.1 μm (mean ± sem, n = 17; Fig. 4(D)). As the lumens of the finest retinal capillaries in the mouse have a diameter of ~6 μm [36], the same diameter as the mouse red blood cell (http://bionumbers.hms.harvard.edu; cf. Fig. 6(D)), the x-y resolution of the AO-SLO can be concluded to be close to 1 μm. In this experiment, the confocal collection aperture (fiber optic) had a diameter of 4 Airy discs.
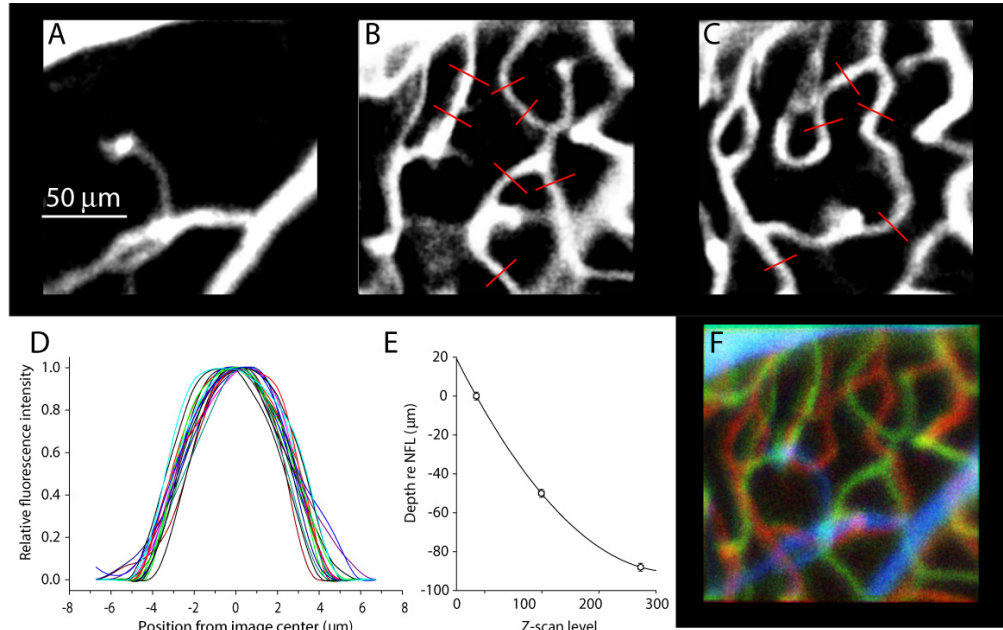
Fig. 4. Fluorescein angiography used to examine AO-SLO resolution and illustrate z-stack acquisition. **A-C**. Selected images from a z-stack of 350 images spanning retinal depth from the large superficial vessels to the capillaries of the outer plexiform layer (cf Fig. 3(C), blue box). The images correspond to stack positions z = 1 (A), z = 148 (B), z = 323 (C), corresponding to the NFL (A), the IPL (B), and OPL (C), respectively, as determined from the corresponding OCT volume (Fig. 3(C), 3(D)). **D.** Fluorescence intensity profiles (n = 17) along lines perpendicular to the smallest capillaries, illustrated in part by the red lines in panels B and C. **E.** Relationship between nominal position in the z-stack (abscissa) and depth in the retina measured in the corresponding pv-OCT image. The smooth parabolic curve fitted through the points was used to interpolate an image stack spaced in micrometers, shown as a "zoom-through" in Media 3. **F.** Depth color-coded projection of the fluorescein angiography images in Media 3; also see Media 4; the same color coding scheme was used as in Fig. 3(D).

3.2.2 Reflectance imaging of axon bundles and microvasculature

While fluorescein angiography can be combined with OCT data to permit precise determination of the axial position of AO-SLO images, it is not desirable to simultaneously apply fluorescence angiography with imaging of fluorescent cells. However, imaging of blood vessels, axon bundles and other retinal structures can also be obtained with AO-SLO reflectance data [37], allowing the depth position of vessels to be matched with corresponding pv-OCT data, and thus the depth of fluorescent cells to be determined. The AO-SLO currently has three imaging channels, two for reflectance (469 nm, 663 nm) and one for fluorescence (excitation, 469 nm). To illustrate the capabilities that these features afford, we compared reflectance images taken at different focus depths with pv-OCT data (Fig. 5).
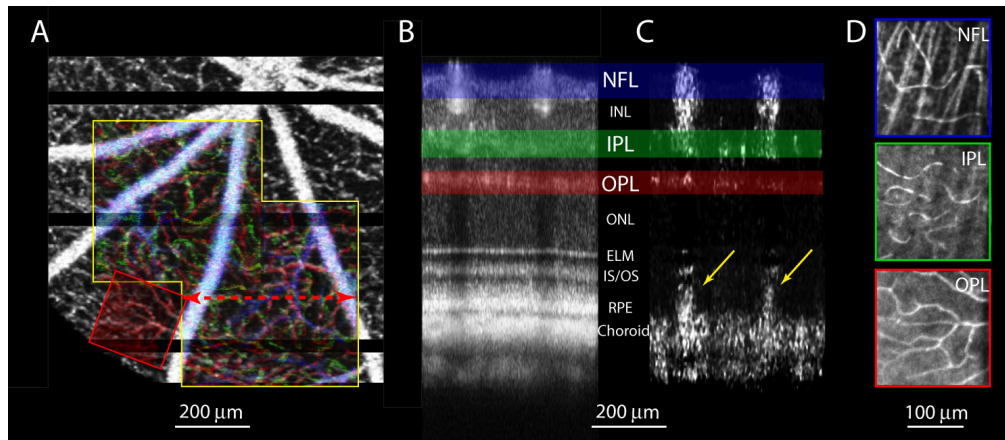
Fig. 5. AO-SLO imaging of microvasculature and depth localization via corresponding pv-OCT imaging. **A.** Digital zoom-in view of lower left quadrant of widefield pv-OCT image (grayscale), with three higher resolution images (color) aligned with and superimposed upon the pv-OCT map. The pv-OCT data acquired during mouse breathing was noisy in this experiment (increasing the pv-OCT signal magnitude), and for presentation clarity was masked (dark black horizontal lines) in the *en face* projection of panel A. The superimposed images are shown with 50% transparency to allow the underlying grayscale image to be seen: the two superimposed RGB-colorized images (yellow boxes) are projections of high resolution pv-OCT volumes, with color indicating depth, while the third image, shown in the red box, is an AO-SLO image, which is also shown in grayscale in the lowermost image (red box) of panel D. **B.** OCT B-scan taken at the dashed red line of panel A. **C.** pv-OCT image corresponding to the B-scan in B. **D.** AO-SLO red reflectance images (663 nm) taken at three focus levels. The layers are identified as the NFL, IPL and OPL respectively (top to bottom) based on the presence of axon bundles, and the progression of changes in the pattern of capillaries. The AO-SLO image identified as OPL was precisely aligned with the OPL layer vessels in 3D in the lower resolution pv-OCT map (red box in panel A). The high resolution pv-OCT images from the immediately adjacent retinal locations (yellow boxes) illustrate the detail available for identifying the 3D location of the AO-SLO image. The pv-OCT image (A) spanned 41 deg (1400 μm); the AO-SLO images span 200 μm x 200 μm. Note that pv-OCT shadow artifacts, marked by yellow arrows in panel C, are present below large retinal vessels in panel C. There is no vasculature in the photoreceptor layers; the phase variance detected there arises from pathlength fluctuations for light passing through fast flowing blood in the large inner retinal vessels.

With the AO-SLO focused on an x-y location found by navigating along a pv-OCT blood vessel map, it was possible to find a precise correspondence between the local capillary bed seen in an AO-SLO reflectance channel image, and a portion of the pv-OCT 3D map (Fig. 5(A)). In reflectance images the blood vessels can be identified as areas of relatively higher reflectance. An alternative analysis that causes the vessels to stand out in strong relief is to process a series of reflectance images taken at a fixed z-position for variation (Fig. 6): an image of the standard deviation unequivocally highlights vessels [38, 39]. Media 5 shows a series of AO-SLO red reflectance images taken at a z-position with OPL focus. In viewing such movies, taken at the 23 Hz frame rate, one is struck by the appearance of blood cell motion in the vessels, though it is difficult to ascertain the direction of motion and its velocity. By analyzing individual frames, and taking advantage of the 14 KHz line scan rate, the velocity of the blood flow could be readily measured, as has been previously show in AO-SLO imaging of the human and mouse retina [40, 41].
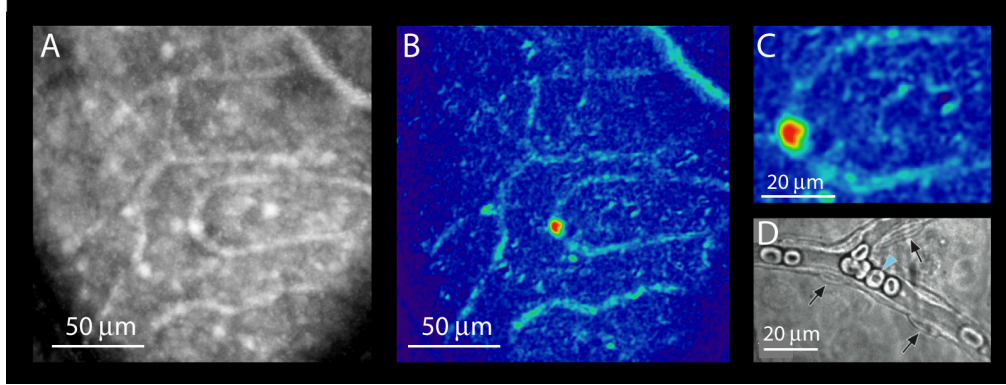
Fig. 6. AO-SLO reflectance imaging of OPL microvasculature. A. Average of 20 successive frames taken with 663 nm reflected light at a focus plane in the OPL. Red blood cell (RBC) motion in the lighter "looping" regions is visualized in Media 5, which plays a series of 147 successive frames. B. Map of the standard deviation of the ensemble of 147 frames shown in pseudocolor, ranging from blue (low s.d.) to red (high s.d.). The red "hotspot" near the center of the image corresponds to a site where the OPL capillary bed connects to that in the IPL: thus in Media 5 RBC's are seen to appear at this location before traversing one of the two OPL capillaries connecting branching from the point. The images in A, B are 200 μm x 200 μm. C. Magnified view of the standard deviation image of B. D. DIC image from preparation of live mouse retina showing capillaries with red blood cells (from [37] with permission).

3.2.3 Measurement of flow in blood vessels with line-scanning

To extract the velocity of flow in blood vessels, we performed interleaved frame- and line-scans with the AO-SLO operating in red reflectance mode (Fig. 7). For larger vessels, it was possible to observe flow in individual x-y frames (data not shown): thus, because each successive line in a frame is taken 71 μs after the previous one, a red-light reflecting red blood cell (RBC) or group of RBCs creates a particle track whose slope in the image is determined by its velocity. The horizontal velocity component V_x of a particle whose track has slope θ (relative the horizontal scan line) is given by

$$V_x(\theta) = -V(45)/\tan(\theta) \tag{1}$$

where $V(45) = 5.5$ mm s^{-1} is the calibrated total x-scan distance (200 μm) divided by the total time for a frame (36.6 ms), i.e., the velocity of a particle whose track has a slope of 45 deg. If the vessel is tilted at an angle α with respect to the scan frame, the actual velocity along the vessel axis is given by

$$V_{axial} = V_x(\theta)/\cos(\alpha) \tag{2}$$

Particle tracks were readily observed in x-t (line) scans (Fig. 7(C), 7(H)) to which Eqs. (1), (2) also apply. We automated the extraction of the particle tracks with a steerable 2D filter analysis (Fig. 7(D), 7(I); Methods, 2.4). The sign of the velocity indicates the direction of flow (negative, rightward; positive, leftward), so that it is possible from the larger vessel map and flow direction to determine whether a given vessel is an artery or vein. For the two vessels illustrated, the mean velocities were $V_x = 9.7 \pm 2.9$ and $V_x = -11.7 \pm 3.6$ mm s^{-1} (mean ± s.d) respectively (Fig. 7(E), 7(J)), negligibly different the axial velocities. Given their positions relative to the optic nerve head (Fig. A, F), both vessels are identified as arteries.
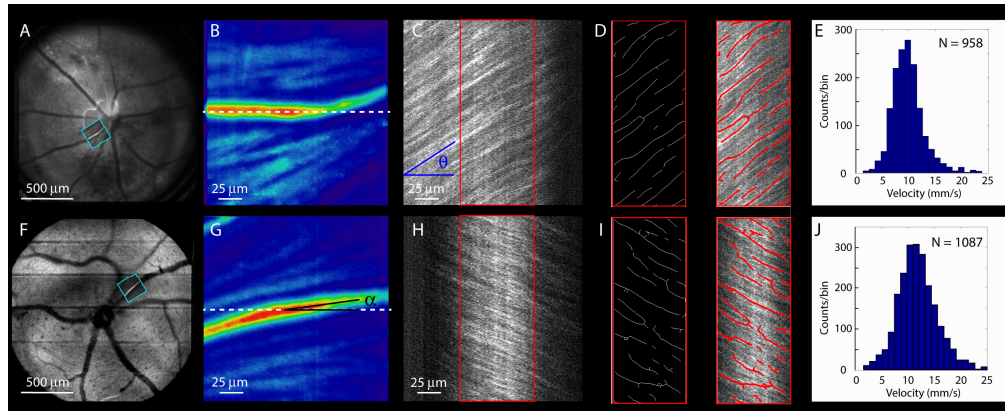
Fig. 7. Measurement of blood flow in mouse retinal vasculature with 663 nm AO-SLO line-scanning. **A, F**: widefield (50 deg) 469 nm reflectance SLO images of two different mice approximately centered on the optic disc. Superimposed are averaged 663 nm AO-SLO reflectance images taken at the locations indicated by the cyan boxes. **B, G**: averaged AO-SLO x-y scans of the cyan-boxed regions in A, F (presented in the "Physics" colormap of ImageJ). The vessels are situated slightly above the neurofibrillary layer, some of whose fibers are seen as pale blue streaks in the background; the AO-SLO focus was set to be approximately in the middle of the vessels. (**C**) and (**H**) show individual frames in a series of linescans (x-t) taken at the midposition of x-y scans, as identified by the white dashed lines in B, G. (**D**) and (**I**) illustrate the automated processing used to extract the particle tracks (see Methods) with the left of each pair of panels showing extracted tracks (white dots) and the right showing an overlay of the tracks (red dots) on the original ROI selected for analysis. (**E**) and (**J**) show histograms of the velocities extracted from the 100- and 81 x-t scans, respectively. The image frames in panels A, B, F, H were 200 μm × 200 μm, and each frame took 0.0366 s to capture. Successive line scans in panels C and H were taken 71 μs apart, at the frequency (14,000 Hz) of the resonant scanner. Media 6 and Media 7 show the entire set of frames in each case, along with the automated extraction of the particle tracks, velocities and histograms.

3.3 AO-SLO imaging of fluorescent microglial and cone photoreceptors cells

3.3.1 Three-dimensional localization of fluorescence microglia cells

Having developed a general method for localizing and characterizing the retinal microvasculature in 3D with pv-OCT and AO-SLO, we applied this method to the localization of fluorescent microglia cells, including widefield (non-AO) SLO imaging because OCT cannot detect fluorescence (Fig. 8). Microglia are a class of non-neuronal cells of great importance for maintenance of the central nervous system (CNS), where they act as "resident macrophages" to clear debris and dying cells. We took advantage of a genetically modified mouse line ($Cx3cr1^{GFP/+}$) that has the coding sequence for EGFP knocked into the genetic locus of the fractaline receptor (Cx3cr1), which is expressed in microglia and macrophages [27]. Widefield SLO reflectance and fluorescence images (Fig. 8(A), 8(B)) and pv-OCT (Fig. 5(A), 8(A)) provided 3D maps of the retina in which AO-SLO images (Fig. 8(C)-8(E)) could be localized within distinct axial focal planes. We first used the red (663 nm) reflectance channel to map the local vasculature and/or neurofiber bundles. The fluorescence excited by 469 nm was then collected, so that its image plane was unequivocally matched to a red reflectance image. Analysis of fluorescence as a function of depth confirmed that microglia reside primarily in the plexiform layers in the healthy retina, as expected from histology [12, 13]. Distinctive patterns of GFP-positive cells and processes were found in the NFL, IPL and OPL (Fig. 8(D)-8(E)). In the OPL the cell branches were tightly planar (Fig. 8(E)), permitting imaging of primary and secondary branches over time without the need for focus adjustment.
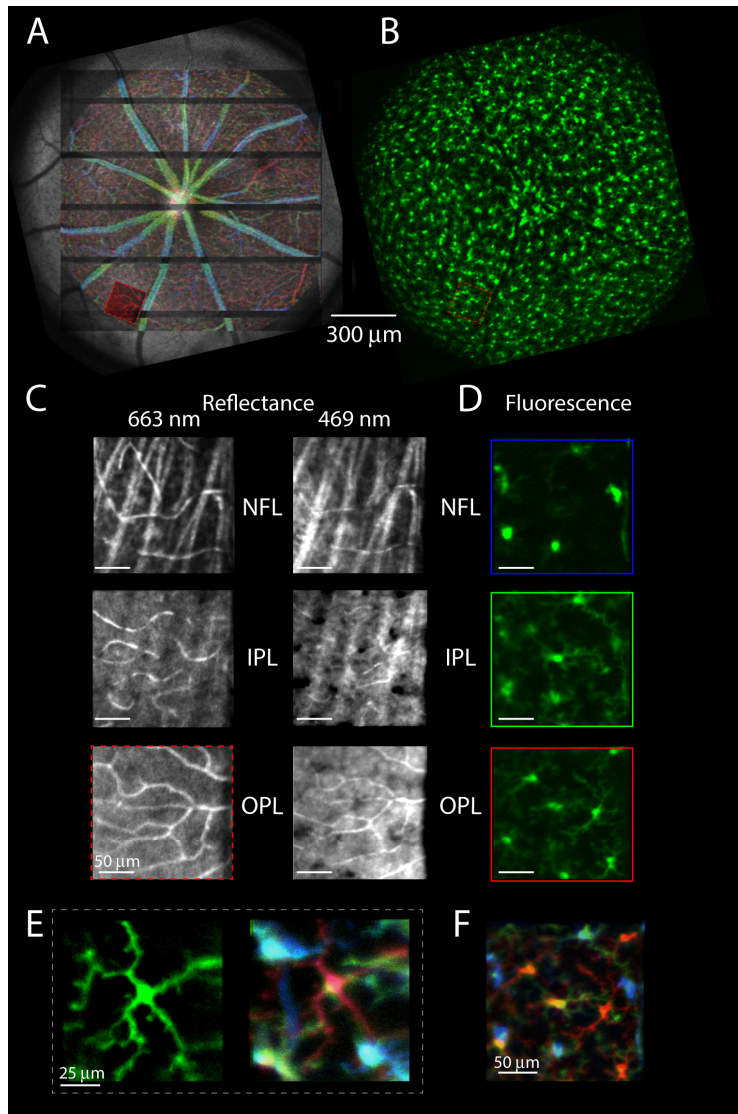
Fig. 8. AO-SLO images of microglia in different retinal layers. **A.** Widefield SLO reflectance image (469 nm) of the same mouse and retina as shown in Fig. 5; the pv-OCT map of Fig. 5(A) (but colorized for depth) has been superimposed upon and aligned with the SLO image, and the location of the AO-SLO imaging region overlaid (red box at 7 o'clock). **B.** Fluorescence image corresponding to panel A, acquired simultaneously with the SLO in a second channel, showing the distribution of microglia across this 50 deg FOV. **C.** AO-SLO reflectance images taken at the NFL, IPL and OPL layers; the OPL image (red box) was taken at the location of the red box in panel A (see also Fig. 5); note that, while less distinct than in the 663 nm reflectance images, the same capillaries are seen in the 469 nm images. **D.** AO-SLO fluorescence images taken with 469 nm excitation at the identical focus position as the 469 nm reflectance images in the corresponding panels in C. Note that the microglia exhibit a distinct pattern in each layer. Images in C, D, F are all from the same 6 deg, 200 μm x 200 μm FOV. **E.** Left: fluorescence image of a single microglia cell located in the OPL imaged in small FOV (3 deg, 100 μm x 100 μm). Right: depth color-coded image of the z-stack from which the fluorescence image at left was obtained, with NFL blue, IPL green, OPL red. **F.** Depth color-coded image of the fluorescence images in panel D; also see Media 8. The color coding scheme is the same as in previous figures, and is represented discretely by the color borders around the images in panel D.

The highly dynamic nature of microglia as they perform their sensing and phagocytic roles under resting and perturbed conditions makes it imperative to study them *in vivo*. Microglia-mediated chronic inflammation has been implicated in a number of disease etiologies, signified by morphological changes in microglia and their migration to the loci of inflammation [42]. This can manifest in the retina as a change from a highly branched to an ameboid shape, including intermediate axial migration through the retinal layers [13], which now should be observable *in vivo* with confocal AO-SLO. The advent of this technique will allow the study of the microglial response to disease and injury, potentially providing necessary *in vivo* proof of the helpful or harmful nature of their activation, opening the door for treatments based on knowledge gained about the role of microglia.

3.3.2 Imaging of cone photoreceptors that express GFP

The cone mosaic of the central human retina and a number of features of human cones *in vivo* have been extensively studied with AO-SLO imaging (reviewed in [1]). While lacking a fovea with a concentrated population of cones, the mouse retina nonetheless has numerous cones, comprising 3% of the total photoreceptor population [43], about the same density as in the human peripheral retina [44]. Mouse cone structure and function have been investigated in many studies [45] and mice have been shown to use their cone vision with high sensitivity in behavioral experiments [46]. As preserving cone function in retinal disease and aging is an important aim of translational research, AO-SLO imaging of mouse cones i*n vivo* is a highly desirable goal. This goal was achieved by imaging cones engineered to express EGFP by intravitreal injection of an adeno-associated virus with a modified capsid (AAV-7M8) carrying the coding sequence of EGFP driven by a cone-specific promoter [28, 30] (Fig. 9). EGFP is a highly soluble protein, whose distribution in cells, including photoreceptors, reflects the water space [47]. The dominant water spaces of mouse cones are the pedicles in the OPL and the cell body and inner segment, which for most cones span the ELM (Fig. 9(A)). Widefield SLO imaging showed numerous green fluorescent spots across the retina in a mouse intravitreally injected several months earlier with AAV-7M8-hlm-EGFP (Fig. 9(C)). The emission spectrum measured in the SLO from small regions centered on bright fluorescent spots was clearly that of EGFP (Fig. 9(F)). The stronger expression of EGFP in the dorsal retina likely reflects the dorso-ventral gradient of M-opsin expression [30, 48, 49]. AO-SLO reflectance and fluorescence data (Fig. 9(E), 9(F)) were collected from several regions of this eye that were previously identified as having puncta of EGFP expression in the combined widefield SLO reflectance and pv-OCT map of the vasculature (Fig. 9(B)).
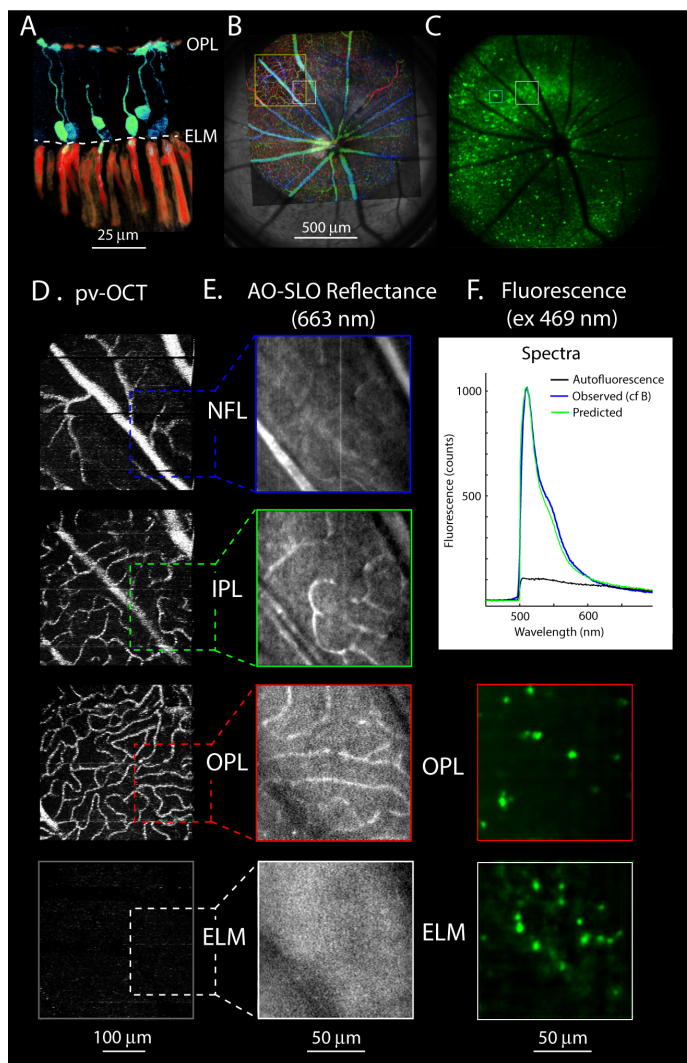
Fig. 9. AO-SLO imaging of mouse cone photoreceptors expressing EGFP. **A.** Confocal image of a live retinal slice of a mouse two months after an intravitreal injection of a capsid-modified AAV vector (AAV-7M8) carrying the coding sequence for EGFP driven by the human L/M-cone promoter (hlm-EGFP). Imaging was performed with a 60X objective; the retina was stained with Alexa555-labeled PNA, which specifically labels cone outer segment sheaths (red). Note that the regions of highest EGFP expression (green) are the cone cell bodies and inner segments (which sit astride the ELM), and the synaptic pedicles, which are in the OPL. **B, C.** Simultaneously acquired widefield SLO reflectance (B) and fluorescence (C) images of another mouse eye transduced with 7m8-hlm-EGFP. A widefield pv-OCT vasculature map color-coded for depth has been overlaid on the reflectance image, and a higher resolution pv-OCT (yellow box) upon it. The white box identifies the region subjected to AO-SLO imaging. **D.** Images segmented from a high resolution pv-OCT volume subtending most of the region that underwent AO-SLO imaging; the region corresponding to the ELM had negligible contrast, arising from the absence of blood vessels. **E.** AO-SLO 663 nm reflectance images, with depth focus corresponding to the adjacent (panel D) pv-OCT images. **F.** *Upper panel*: Emission spectrum (blue trace) obtained by scanning the region shown in the cyan box in C with 469 nm light. An autofluorescence spectrum (black trace) was obtained from a region with negligible green fluorescence. The observed emission spectrum (blue trace) was predicted (green trace) by summing a scaled EGFP emission spectrum [10] with the autofluorescence spectrum. *Lower panels*: AO-SLO fluorescence images with focus at same retinal depth as the corresponding adjacent red reflectance channel images.

To identify the depth of origin of the fluorescence signals, we co-registered the microvasculature as visualized with the red reflectance AO-SLO data with the zoomed pv-OCT volumetric vascular maps (Fig. 9(D)). In this mouse, while focused at the ELM we did not observe the photoreceptor mosaic previously observed in the mouse [4]. As we have observed the mosaic in other mice (data not shown), its absence in the reflectance image likely arises from relatively high 469 nm scattering and inadequate averaging. We interpret the fluorescent spots seen with an ELM focus as arising from cone cell bodies and inner segments (Fig. 9(A)), and those with an OPL focus as arising from cone pedicles. That these two sets of spots have a distinct pattern likely reveals that the pedicles are not in alignment with the cell bodies along the axis of light propagation. Orderly transmission of spatial information from the photoreceptor mosaic does not require axial alignment of the synaptic region of the cell with the inner and outer segment, which guide and capture light. Human foveal cone pedicles, for example, are laterally displaced by hundreds of micrometers from the cone cell bodies. This, and many other issues about the spatial distribution and optical properties of mouse cones should be addressable with this approach, which enables the precise location of some cones to be unequivocally determined.

4. Summary and discussion

We have presented a framework for imaging the mouse retina in which cells and structures visualized with high resolution, small field-of-view AO-SLO can be localized in 3D with respect to widefield pv-OCT and SLO reflectance and fluorescence images. We think that sequential pv-OCT, SLO and AO-SLO imaging has great utility for investigating mouse models of ocular disease at the cellular level. Using multiple independent modalities enables unequivocal localization of cells in the living retina. We used this framework to characterize the volumetric morphology of blood vessels from the largest size to the capillary level, and to achieve depth-resolved AO-SLO fluorescent images of microglia and cone photoreceptors expressing EGFP. To evaluate performance of this methodology three mouse variants were imaged: (1) wild type mice; (2) mice with EGFP-labeled microglia cells; and (3) mice with EGFP-labeled cones. In each case we have demonstrated precise localization of retinal cells and/or microvasculature imaged with AO-SLO in the large field-of-view volumes.

One advantage of this multi-modal and multi-scale imaging approach is that OCT and SLO provide rapid, widefield screening and mapping of retinal morphology. Such screening is essential in following cellular structures across the retina during disease progression, or for delivering and testing treatments. AO-SLO alone allows confocal imaging with a depth of focus of approximately 5 μm, and thus, in theory any axial position of a cell or structure could be measured with respect to the reference layers (NFL or ELM) by driving the focus through the retina with the deformable mirror. In practice, however, such focal shifting is non-linear with the AO-system defocus offset, and the AO-correction could change if the retina undergoes structural changes that alter the reflectivity or thickness of any retinal layers. In contrast OCT provides inherently precise depth information that doesn't depend on any of the above mentioned factors. Additionally, prior imaging with OCT and SLO allows us to assess the quality of the mouse eye's optics and select regions of interest (ROI) to be investigated with AO-SLO. Our AO-SLO system implements wavefront sensor-based AO correction and uses reflective afocal design to minimize system aberrations and pupil wander during scanning. These are the same principles used in the AO-SLO of Geng et al. [4]. The main difference between these two approaches is the location of the wavefront corrector with respect to the scanning mirrors and the use of the wavefront beacon for imaging, achieved by changing the wavefront beacon focal plane position.

The AO-SLO was employed in reflectance mode to image retinal blood vessels, including capillaries, whose distinct patterns provide fiducial markers for co-localization of fluorescent cells. We also used AO-SLO reflectance to measure blood flow in mouse retinal vessels, as

has previously been demonstrated in human AO-SLO imaging. Application of such flow analysis promises to provide new insight into mouse models of vascular disease.

In this manuscript we also describe initial efforts to apply AO-SLO to localize microglia within specific retinal layers. Additional work will be needed to obtain the precise 3D position of each microglia cell with respect to nearby capillaries, veins or arteries. Ongoing research on microglia with a larger sample of mice is underway to address these and other issues, including microglia motility and mobility. A mouse model in which an AAV vector was used to drive EGFP expression in cones was used to demonstrate AO-SLO axial sectioning capabilities within the photoreceptor layer. When photoreceptors were visualized in the fluorescence channel no mosaic was observed in the back-reflected channel. More studies are needed to assess whether there are morphological changes affecting AO correction or reflectivity of photoreceptors transduced with the virus.

5. Conclusion

Widefield SLO and OCT imaging offer an efficient and robust screening assessment of retinal structures, but lack the axial resolution (SLO) or fluorescence detection capability (OCT) for studying individual cells in 3D. Combining AO-SLO with widefield SLO and OCT imaging enhances the interpretation of AO-SLO data, makes it easier to focus AO-SLO resources on specific retinal locations and cellular targets, and can help to optimize the timing of AO-SLO data acquisition with respect to dynamic processes such as rapid retinal degeneration [13].

Acknowledgments